A first-principles and thermodynamics study of compositionally-tuned complex metal oxides: Cation release from the (001) surface of Mn-rich lithium nickel manganese cobalt oxide.

Joseph W. Bennett[1], Diamond Jones[1], Robert J. Hamers[2] and Sara E. Mason[1]*

1: Department of Chemistry

University of Iowa, Iowa City, Iowa 52242;

2: Department of Chemistry

University of Wisconsin-Madison, Madison, WI 53706

E-mail: sara-mason@uiowa.edu

*To whom correspondence should be addressed

Abstract

Compositional tuning of nanoscale complex metal oxides (CMOs) can lead to enhaced performance and favorable properties for a variety of energy related applications. However, investigations of the nanoscale CMOs used in energy storage technologies demonstrate that these nanomaterials may have an adverse biological impact, highlighting a fundamental knowledge gap between nanomaterial design and the structure and properties at the end of life. CMO nanomaterials can enter the environment due to improper disposal, where they undergo subsequent (as of yet poorly understood) nanoscale transformations that may affect biological response and ultimately, environmental fate. This points to the need for studies at the nano-bio interface that can be used to shape rules for the redesign of CMOs: materials that are are potentially more benign by design and serve as examples of sustainable nanotechnology. The example given here is to enrich lithium nickel manganese cobalt oxide, $Li_x(Ni_yMn_zCo_{1-y-z})O_2$ (NMC) with Mn to create a family of materials that are less expensive and potentially less toxic to a wide range of organisms. In this manuscript, we investigate the structure and electronic states of Mn-rich NMC at the density functional theory (DFT) level to elucidate the interplay of redox properties, oxidation state, and coordination environment of a compositionally-tuned CMO. We find that the oxidation states of Ni and Co remain mostly unaffected while Mn exists as both Mn^{2+} and Mn^{4+}. Our models show that the ratio of Mn^{2+} and Mn^{4+} varies with changes in the coordination environment, such as the identity of neighboring atoms and surface OH group coverage. The surface metal release properties of Mn-rich NMC compositions are predicted using a DFT + solvent ion model, and show that Mn-rich NMC compositions are inherently more prone to dissolution than NMC, and that this is attributed to the changes in oxidation state of the transition metals in Mn-rich NMC.

Introduction

The rapid rise in renewable energy is leading to increased use of complex metal oxides (CMOs) in large quantities, with current manufacturing capacities estimated to be at least 100,000 metric tons/year.[1,2] While in many cases these materials are being used as nanomaterials, mechanical stresses during use lead to pulverization and subsequent formation of nanoparticles from bulk materials.[3] In particular, the intercalation materials in lithium ion batteries (LIBs) are CMOs that contain potentially toxic transition metals,[4–7] leading to questions about how to re-design nanoscale materials to reduce adverse biological impact. Recently it has been argued that the environmental impact of engineered nanomaterials is small.[8] However, others have argued that the statistical methods and analysis in that work were flawed.[9] In either case it is important to recognize that these and other studies[10–13] have generally focused attention on a small subset of relatively simple binary metal oxides, such as TiO_2 and SiO_2, that are inherently chemically stable. In contrast, the recent increases in LIB use have now made worldwide manufacturing of CMO materials such as $Li(Ni_xMn_yCo_{1-x-y})O_2$ (NMC) comparable to or even greater than the nanomaterials considered in Refs.,[10–13] with projected Co manufacturing estimates of up to 150,000-300,000 metric tons/year through 2025.[2] It has been shown that multi-valent mixed transition metal oxides can be tuned to obtain desirable properties in a CMO, but what is not yet clear is how compositional tuning will affect the interplay of redox properties, oxidation state and coordination environment in bulk CMOs, let alone the surface.[14,15]

Since NMC materials contain transition metals with known toxicity[4,6,7,16] but have poorly understood chemical transformations, there remains a mandate to understand the factors that influence metal release and to identify factors that can mitigate the potentially adverse risks associated with unintentional release into the environment.[17] In prior studies, we have shown that NMC transformed incongruently; releasing Li, Ni and Co to aqueous media, leaving behind a Mn-rich shell. It was also shown that the released Ni and Co ions inducing toxicity in *Shewanella oneidensis* MR-1 and *Daphnia magna*.[4,7,16] Billy and co-workers reported a similar incongruent metal release from NMC in highly acidic solutions, and proposed a mechanism based on experimental

observations.[18] These previous studies suggest that Mn-enriched particles have greater stability in aqueous environments, and that a more complete mechanistic understanding of the transformations of CMOs remains lacking. Recent reviews identify the need for exploration and design of new CMO with lower cost and increased sustainability. Mn is a redox active TM that is cheaper than Co, more Earth abundant, and environmentally friendly, side-stepping concerns about cost, scarcity, and adverse biological impact.[14,15,19]

Using first-principles to assess how the surface of a CMO behaves for a wide range of tunable conditions will allow for insights into energy storage/production technologies such as oxygen reduction/evolution catalysts, electrochemical capacitors, and fuel cells, potentially leading to increased efficiencies and different operating regimes beyond current CMO capabilities.[14] Moreover, the results of these analyses could be used to form sustainable design principles for tunable CMO materials such as spinels, pyrochlores, and perovskites with rich, complex chemistries,[15,20,21] and be used to control the interactions and transformations underlying the adverse biological impact of CMOs.[22–24] Recently, a new approach has emerged to calculate the thermodynamics associated with metal release from complex oxide materials. The DFT + solvent ion model[25] was used to understand the surface transformations that may take place, over a wide range of tunable conditions for $LiCoO_2$ (LCO)[26] and the related NMC[27] material. In these studies, metal release thermodynamics was approximated as the initial stage of material dissolution. The quantity of interest in these studies was the free energy of release of surface metal species, referred to as dissolution, ΔG_{diss}. ΔG_{diss} was computed using a piecewise approach that combined DFT total energies (ΔG_1) with tabulated values of G^0_{SHE} and experimentally controllable parameters (ΔG_2). This thermodynamic approach demonstrated that in aqueous environments, Li and H will exchange at the surface, and that surface metal release was most likely OH mediated. The experimentally observed trend in metal release, as interpreted from ICP measurements,[4,16] is that Li $>$ Ni $>$ Co $>$ Mn, which agreed with the empirical trend obtained with the DFT + solvent ion values for ΔG_{diss}. All together, the agreement between theory and experiment, along with physical insights provided by the DFT + solvent ion model offers a platform for understanding the mechanisms of CMO transformations

and using this information to create and test new materials design rules.

Here we use first-principles DFT and thermodynamics to explain the observed metal release trends in Mn-rich NMC through an analysis of the surface coverage, coordination environment, and electronic structure. We model Mn-rich NMC compositions of chemical formula $Li_x(Ni_{0.22}Mn_{0.56}Co_{0.22})O_2$ and $Li_x(Ni_{0.11}Mn_{0.78}Co_{0.11})O_2$, and calculate values of ΔG_{diss} to compare with previous results obtained from modeling $Li_x(Ni_{0.33}Mn_{0.33}Co_{0.33})O_2$.[27] We find that the local environment, in terms of neighboring transition metals, surrounding pH, and surface terminations will change the redox properties of the surface transition metals, which will affect the release of transition metals from Mn-rich NMC surfaces. Our results, for a wide range of compositions and chemical environments, can also be used as input parameters for improved environmental fate and toxicity models[28,29] and as a guide for the redesign of CMOs with tunable redox properties.

Materials and Methods

Periodic DFT calculations[30,31] of Mn-rich NMC surface structures are employed using Quantum Espresso, an open source software package.[32] All atoms are represented using ultrasoft GBRV-type pseudopotentials,[33,34] and all calculations use a plane-wave cutoff of 40 Ry for the wavefunction and 320 Ry for the charge density. All atoms are allowed to relax during structural optimizations, and the convergence criteria for self-consistent relaxations was a maximum residual force of 5 meV/Å per atom. Calculations are performed at the GGA level[35] using the PBE-GGA exchange correlation functional. A comparison of cation release using GGA and GGA+U methodology is presented in the Supplemental Materials of Ref.;[27] we found that the addition of Hubbard U (above $\approx$ 2 eV) to each of the transition metals in NMC resulted in non-linear behavior in ΔG_1. This changed the trend in release from Ni $>$ Co $>$ Mn to Co $>$ Ni $>$ Mn, which is why GGA + U methodology is not employed in the current study.

Prior experimental work described the as-synthesized NMC nanosheets as having at least seven O-TM-O layers,[4] which would be computationally expensive for the supercell compositions that

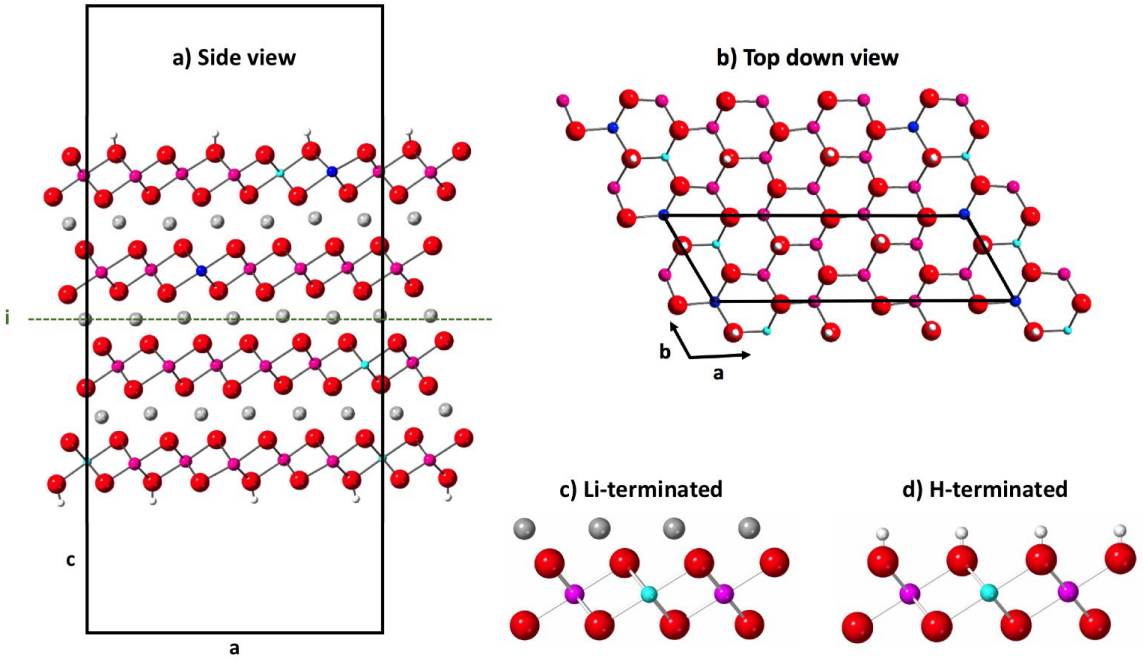

Figure 1: Shown here for the Mn-rich NMC supercell NMC-171-A are the a) side view and b) top down view of an H-terminated surface slab, with both crystallographic axes and inversion center (*i*, side view) labeled. In the bottom right hand corner, truncated versions of the c) Li-terminated and d) H-terminated surface layer are depicted to illustrate differences in preferred location. Li is depicted as gray, H is white, and O is red. The transition metals in the subsurface layer are depicted as follows: Ni is dark blue, Mn is magenta, and Co is cyan.

we are investigating. Therefore, the Mn-rich NMC surface slabs used here include four total transition metal oxide layers (O-*TM*-O), like the NMC surfaces in Ref.,[27] of which the two interior and two exterior layers are related by inversion symmetry, as has been shown to be a best practice.[36] Top and side views of supercell surface slabs are shown in Figure 1. The surfaces are a $[\sqrt{3} \times \sqrt{3}]$R30^o rotated modification of the LCO unit cell and both side and top down views of a representative Mn-rich NMC supercell surface slab are shown in Figure 1. Highlighted in Figures 1 for (c) Li and (d) H-terminated surfaces are the differences between the two surface terminations. Li is above a 3-fold hollow site and H is above an O, forming an OH bond. Each supercell surface slab has in-plane dimensions of $3\sqrt{3}a \times \sqrt{3}a$ (where a=2.883 Å), and at least 15 Å of vacuum between surface slabs. This yields total cell dimensions of 14.981Å $\times$ 4.994Å $\times$ 41.048Å. Surface relaxations use a 2$\times$6$\times$1 k-point grid,[37] which converges the energy sampling to within 10 meV per formula unit. Since each Mn-rich NMC layer has 9 total transition metal (*TM*) sites,

removal of 1 TM from a surface results in a surface vacancy density of 1/9 or 11.11%. This is kept constant for all calculations. The two compositionally-tuned slabs are labeled 171 and 252, where 171 refers to transition metal compositions of $Ni_{1/9}Mn_{7/9}Co_{1/9}$ (11%Ni-78%Mn-11%Co) and 252 refers to transition metal compositions of $Ni_{2/9}Mn_{5/9}Co_{2/9}$ (22%Ni-56%Mn-22%Co), close to the stoichiometries of the synthesized materials discussed in Ref.[6]

We investigate three distinct cation arrangements for the 171 and 252 compositions, labeled A, B, and C. These surfaces form a representative set in which the oxidation state and coordination environment (via atomistic interactions such as neighboring atoms and surface terminations) can be compared. Each TM removed will have a subscript with the number of Mn nearest neighbors and a superscript with the number of Ni and/or Co nearest neighbors. For example, removing the Ni from 171-B with 2 Co and 4 Mn neighbors (Depicted in Figure 2b) would be referred to as removing 171-B-Ni^{2Co}_{4Mn}, and differentiable from removing a Ni from 252-C with 1 Co and 5 Mn neighbors (depicted in Figure 3c) which would be referred to as removing 252-C-Ni^{1Co}_{5Mn}. It should be clarified that not every TM is removed from each surface, but a representative set to map out the breadth of TM release from Mn-rich NMC as the first step in material dissolution.

The perfectly alternating $Ni_{1/3}Mn_{7/3}Co_{1/3}$ (33%Ni-33%Mn-33%Co) composition, referred to as 333, contains Ni with 3 Mn and 3 Co nearest neighbors (333-Ni^{3Co}_{3Mn}), Co with 3 Mn and 3 Ni nearest neighbors(333-Co^{3Ni}_{3Mn}), and Mn with 3 Co and 3 Ni nearest neighbors (333-$Ni^{3Co-3Ni}_{0Mn}$). In all DFT surface calculations, Ni and Co atoms are initialized spin-down and spin-up, respectively. To maximize antiferromagnetic spin coupling, for 171-NMC, of the seven Mn, four are initialized spin-up and 3 are initialized spin-down, and for 252-NMC, of the five Mn, three are initialized spin-up and two are initialized spin-down.

Here we model surface metal release (as the initial step of dissolution) by removing a transition metal, O, and H from the surface. We assume that the removal of any M-OH species results in a delocalization of electrons, since operation of Li-ion batteries relies upon the oxidation/reduction response of redox active TM in the cathode. To compute the change in free energy of metal dissolution, ΔG_{diss}, a DFT + solvent ion method[25,38] based on Hess's Law is employed. In the

DFT + solvent ion method, ΔG_{diss} is partitioned between the computed energies of the reactants and products (used in ΔG_1) and experimental data (used in ΔG_2). Zero-point energy (ZPE) correction terms are added to the DFT total energies of NMC slabs to obtain $\Delta G_1 = E_{\text{products}} - E_{\text{reactants}} + \text{ZPE}$, as described in Ref.[27] and in the style on Ref.[25] The total energies of M, O, and H released from the surface are for the atoms in their standard state, which implies that ΔG_1 can be used as a term that gauges relative lattice stability for the removal of an isolated TM-OH unit per surface slab.

The second model term, ΔG_2, is based on the Nernst equation. $\Delta G_2 = \Delta G^0_{\text{SHE}} - n_e e U_{\text{SHE}} - 2.303 n_{\text{H}^+} \text{kT pH} + \text{kT ln a}(\text{H}_x\text{AO}_y^{z-})$, where ΔG^0_{SHE} is the change in free energy of the aqueous cation/anion relative to the standard state, referenced to the standard hydrogen electrode (SHE). eU_{SHE} is the applied potential, relative to the SHE, and $\text{H}_x\text{AO}_y^{z-}$ are the concentrations of the released aqueous ions. Here we assume that no external potential is applied (eU_{SHE}=0) and that ion concentrations are 1×10^{-6}M, an order of magnitude in line with measurements of released cations reported in experiment.[4,6] n_e and n_{H^+} are the number of electrons and protons involved in the chemical reactions required for surface release. They are zero for the Li^{1+}, Ni^{2+}, Mn^{2+}, and Co^{2+} aqueous species in the pH region of 1 to 9 investigated here.

Values of ΔG^0_{SHE} are obtained from Ref.[39] and are tabulated in units of eV in Section S1 of the supplemental materials. At conditions of $eU_{\text{SHE}} = 0$ and $a = 1\times10^{-6}$M, DFT-calculable Pourbaix diagrams[40] show that $\text{Ni}^{2+}_{(\text{aq})}$ (ΔG^0_{SHE} = -0.472 eV) will be the preferred aqueous cation of Ni until ≈ pH 9.5 when $\text{NiO}_{(\text{s})}$ will precipitate, $\text{Mn}^{2+}_{(\text{aq})}$ (ΔG^0_{SHE} = -2.363 eV) will be dominant until ≈ pH 10, when $\text{Mn}_2\text{O}_{3(\text{s})}$ or $\text{Mn}_3\text{O}_{4(\text{s})}$ will precipitate, and $\text{Co}^{2+}_{(\text{aq})}$ (ΔG^0_{SHE} = -0.563 eV) will be dominant until pH 7, where $\text{Co}^{2+}_{\text{aq}}$ reacts further with H_2O to produce $\text{HCoO}^{-1}_{2(aq)}$ (ΔG^0_{SHE} = -4.223 eV), which becomes the preferred aqueous ion of Co. In the pH region investigated here (pH 1 to 9), the dramatic change in Co speciation, $\text{Co}^{2+}_{(\text{aq})}$ vs. $\text{HCoO}^{-1}_{2(aq)}$, will be present as a discontinuity at pH 7.

It is clear from the ΔG^O_{SHE} values that the speciation of the metals after release depends on identity and conditions, the former which we infer from Pourbaix diagrams and the latter which can be parametrically tuned in the calculation of ΔG_2. It is important to emphasize that the hydrated

metal species are not being calculated using DFT, and are instead captured entirely in ΔG_2. One of the main objectives of this work is to investigate the release of Mn-rich NMC materials for a range of environmentally relevant conditions. Choosing a wide pH range allows for release comparisons of the divalent *TM* cation species Ni^{2+}, Mn^{2+}, Co^{2+} in environments as diverse as acid-mine runoff, water wells, and lakes and streams. Example calculations of ΔG_{diss} from 333-NMC are presented in Section S1 of the Supplemental Materials of Ref[27] and Section S1 of the supplemental materials of the present work.

Results and Discussion

171 and 252 Surface Models

For the 171-NMC (11% Ni-78% Mn-11% Co) compositions depicted in Figure 2, the arrangement of neighbors in the supercell slabs allows for control of the distance between Ni and Co. These slabs can be used to determine how the local environment of an isolated *TM* can influence the release of each species and how changes in coordination affect both the oxidation state and the electronic band structure for all *TM* species.

For surfaces A-C, the distance between Ni and Co is let increase by at least 2.00 Å. As shown in the top views of Figure 2, 171-A has a repeat unit of Mn-Ni-Co-Mn-Mn-Mn-Mn-Mn-Mn (where Ni and Co are nearest neighbors), and Ni and Co are separated by 2.96 Å. This is in close agreement to the DFT-relaxed lattice constants of both bulk LCO (2.85 Å)[26] and NMC (2.88 Å).[27] 171-B has a repeat unit of Mn-Ni-Mn-Co-Mn-Mn-Mn-Mn-Mn (where Ni and Co are next-nearest neighbors, separated by one Mn, or 5.00 Å apart), and 171-C has a repeat unit of Mn-Ni-Mn-Mn-Co-Mn-Mn-Mn-Mn (where Ni and Co are separated by two Mn, or 7.59 Å apart). These arrangements allow for a comparison of ΔG_{diss} of Ni and Co between surfaces, and Mn from the same surface. For example, the release of a Ni with 4 Mn and 2 Co neighbors (171-A-Ni^{2Co}_{4Mn}) can be compared to that of a Ni with 6 Mn and 0 Co neighbors (171-C-Ni^{0Co}_{6Mn}) in *different* surfaces, and the release of the Mn with 3 Mn, 2 Ni, and 1 Co neighbors (171-A-$Mn^{2Ni-1Co}_{3Mn}$) can be compared to that of a Mn

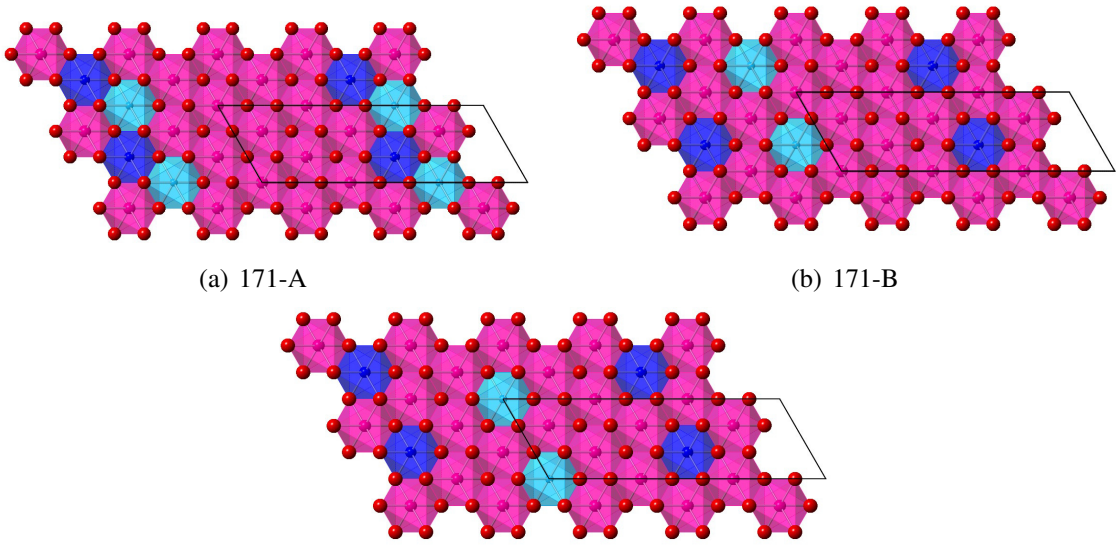

(a) 171-A (b) 171-B

(c) 171-C

Figure 2: Top-down views of the 171 Mn-rich NMC surfaces, where the distance between Ni (dark blue) and Co (cyan) octahedra is systematically adjusted from a) nearest neighbor, to b) next nearest neighbor, separated by one Mn (magenta) neighbor, and finally c) Ni and Co separated by two Mn.

with 6 Mn and no Ni or Co neighbors (171-A-$Mn_{6Mn}^{0Ni-0Co}$) in the *same* surface.

Depicted in Figure 3 are the top views of the 252 Mn-rich NMC supercell surface slabs, of composition 22% Ni-56% Mn-22%Co. 252-A has a repeat unit of Mn-Ni-Co-Mn-Ni-Mn-Mn-Mn-Co, 252-B has a repeat unit of Mn-Ni-Mn-Mn-Co-Ni-Mn-Mn-Co, and 252-C has a repeat unit of Mn-Ni-Co-Mn-Mn-Co-Mn-Ni-Mn. The design of these supercell slabs allow for comparisons of TM that have atomic arrangements similar to 333-NMC than 171-NMC, but in a different extended chemical environment. For example, removing 252-A-Co_{3Mn}^{3Ni} should yield a ΔG_{diss} more similar to 333-Co_{3Mn}^{3Ni}, than either 252-B-Co_{4Mn}^{2Ni} or 252-C-Co_{4Mn}^{2Ni}, which themselves should behave similarly.

As mentioned in the Introduction and Materials and Methods, prior studies have demonstrated that CMO surfaces in contact with aqueous media will undergo Li-H exchange to become H-covered. This results in an OH functional group termination on the CMO surface. In this work, surface coverages to compare ΔG_{diss} will be either 1/3 or 2/3 OH-terminated,[26,27] and top down views showing the different coordination environments are depicted in Figure 1.

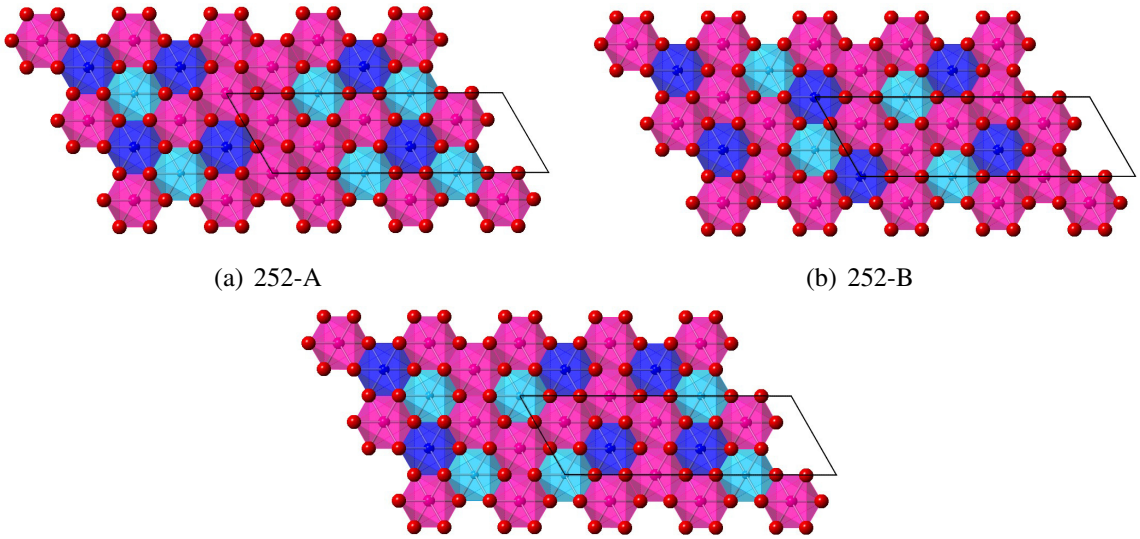

(a) 252-A (b) 252-B

(c) 252-C

Figure 3: Top views of 252 NMC compositions. Same color scheme as Figure 1.

Metal Release From Mn-rich NMC

The initial reference structure for each of the 171 and 252 surface metal release calculations will be a 1/2 Li-terminated surface. Since 1/2 Li-terminated surfaces cannot be created with a $3\sqrt{3}a \times \sqrt{3}a$ surface slab, the average total energy of a 1/3 and 2/3 Li-terminated surface will be used to compute ΔG_{diss} in each case. Inspection of Figure 4 shows that ΔG_{diss} of Ni (a), Co (b), and Mn (c) is dependent on composition and surface termination. The slope of 1/3 H surface coverage (dot-dashed lines) is less than 2/3 H surface coverage (solid lines), indicating that NMC surfaces with less H will be more stable at higher pH than NMC surfaces with more H. The magnitude of ΔG_{diss} from NMC-171 is similar for Ni, Co, and Mn for all pH below 7, and then switches to Ni $>$ Co $>$ Mn. The difference in ΔG_{diss} between 171 and 252 compositions increases in the following order: Ni $<$ Co $<$ Mn. Ni release is the least sensitive to changes in composition and surface termination, while Mn is the most sensitive. This is opposite the trend observed in NMC-333, demonstrating that trends in metal release are highly dependent upon coordination environment.

There are general trends present in the ΔG_{diss} values in Table 1. As Mn content is increased relative to Ni and Co, the DFT + solvent ion model predicts surface metal release to be more

Table 1: ΔG_{diss} of Ni, Co, and Mn from NMC surfaces with 1/3 H coverage for pH 3, 5, 7, and 9. Entries are ordered by compositions 171, 252, and 333 and the number of Mn nearest neighbors.

cation	ΔG pH 3 (eV)	ΔG pH 5 (eV)	ΔG pH 7 (eV)	ΔG pH 9 (eV)
171-B-Ni^{0Co}_{6Mn}	-6.43	-5.95	-5.48	-5.01
171-C-Ni^{0Co}_{6Mn}	-6.33	-5.86	-5.39	-4.92
171-A-Ni^{2Co}_{4Mn}	-6.01	-5.54	-5.06	-4.59
252-C-Ni^{1Co}_{5Mn}	-5.46	-4.63	-3.81	-2.98
252-B-Ni^{1Co}_{5Mn}	-5.18	-4.71	-4.24	-3.77
252-A-Ni^{1Co}_{5Mn}	-4.98	-4.51	-4.04	-3.57
252-B-Ni^{2Co}_{4Mn}	-5.52	-5.05	-4.58	-4.10
252-C-Ni^{2Co}_{4Mn}	-4.93	-4.46	-3.99	-3.52
333-A-Ni^{3Co}_{3Mn}	-2.81	-2.34	-1.87	-1.39
171-B-Co^{0Ni}_{6Mn}	-6.10	-5.63	-5.15	-9.94
171-C-Co^{0Ni}_{6Mn}	-5.97	-5.50	-5.03	-9.81
171-A-Co^{2Ni}_{4Mn}	-5.31	-4.83	-4.36	-9.15
252-B-Co^{1Ni}_{5Mn}	-4.23	-3.77	-3.29	-8.07
252-C-Co^{1Ni}_{5Mn}	-4.28	-3.81	-3.34	-8.12
252-B-Co^{2Ni}_{4Mn}	-4.98	-4.51	-4.04	-8.82
252-C-Co^{2Ni}_{4Mn}	-4.75	-4.28	-3.80	-8.59
252-A-Co^{3Ni}_{3Mn}	-3.86	-3.39	-2.92	-7.70
333-A-Co^{3Ni}_{3Mn}	-2.09	-1.62	-1.15	-5.93
171-B-$Mn^{0Ni-0Co}_{6Mn}$	-5.11	-4.64	-4.17	-3.70
171-A-$Mn^{0Ni-1Co}_{5Mn}$	-5.56	-5.09	-4.62	-4.14
171-B-$Mn^{1Ni-0Co}_{5Mn}$	-6.59	-6.12	-5.64	-5.17
171-C-$Mn^{1Ni-1Co}_{4Mn}$	-5.51	-5.04	-4.57	-4.09
171-A-$Mn^{1Ni-2Co}_{3Mn}$	-6.27	-5.80	-5.33	-4.86
252-B-$Mn^{2Ni-2Co}_{2Mn}$	-4.15	-3.68	-3.20	-2.73
252-A-$Mn^{2Ni-3Co}_{1Mn}$	-3.92	-3.45	-2.98	-2.50
252-C-$Mn^{3Ni-1Co}_{2Mn}$	-3.61	-3.13	-2.66	-2.18
333-A-$Mn^{3Ni-3Co}_{0Mn}$	-1.28	-0.81	-0.34	-

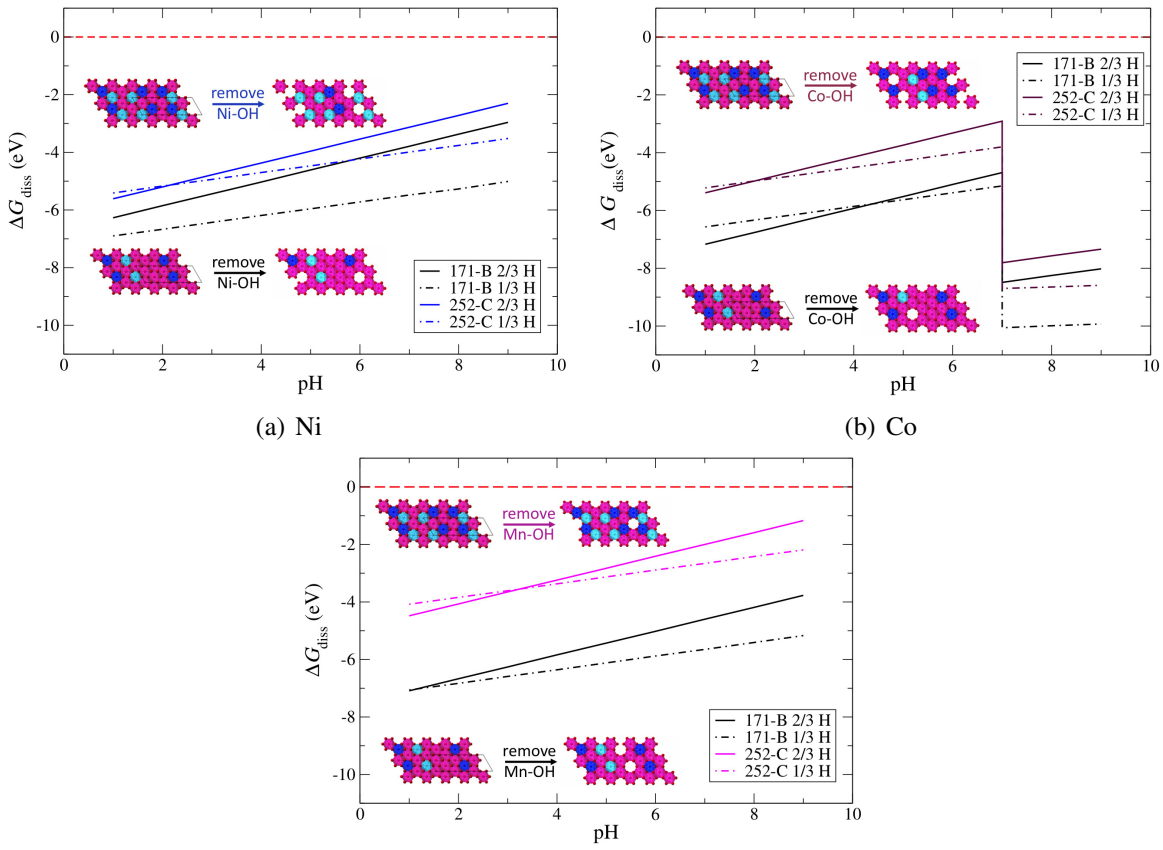

(a) Ni (b) Co

(c) Mn

Figure 4: ΔG_{diss} of a) Ni, b) Co, and c) Mn for both 1/3 and 2/3 H-terminated NMC surface slabs 171-B and 252-C. In all plots, the solid lines are used for 2/3 H surface coverage and dot-dashed lines are used for 1/3 H surface coverages. The dashed red line at ΔG_{diss}=0 separates the region where metal release is predict to be favored ($\Delta G_{\text{diss}} < 0$) from the region where it is not predicted to be favored ($\Delta G_{\text{diss}} > 0$).

favorable for all pH. On average, cation release will occur more readily for 171-NMC compositions than 252-NMC compositions, and will occur more readily for 252-NMC compositions than 333-NMC compositions. At the 11% Ni/Co content of 171-NMC, compositional tuning adjusts the preferred trend in cation release from the Ni > Co > Mn observed in the 252 and 333-NMC compositions to Ni > Co $\approx$ Mn.

Specific comparisons of cation release can also be made from the data in Table 1. The lowest ΔG_{diss} values of the complete set are $\text{Mn}_{5\text{Mn}}^{1\text{Ni}-0\text{Co}} > \text{Ni}_{6\text{Mn}}^{0\text{Co}} > \text{Mn}_{3\text{Mn}}^{1\text{Ni}-2\text{Co}} > \text{Co}_{6\text{Mn}}^{0\text{Ni}} > \text{Ni}_{4\text{Mn}}^{2\text{Co}}$. An atomistic insight from this type of comparison is that cations surrounded by three or more Mn are more likely to be released from the surface than cations in a perfectly alternating NMC-333 like

pattern. One can obtain further insights by comparing subsets of the full set of cations. Focusing on Co, ΔG_{diss} of $\text{Co}^{\text{1Ni}}_{\text{5Mn}}$ is similar between different surfaces (252-B and 252-C, 0.05 eV), but changing the nearest neighbors of Co from $\text{Co}^{\text{1Ni}}_{\text{5Mn}}$ to $\text{Co}^{\text{2Ni}}_{\text{4Mn}}$ in the same surface can increase ΔG_{diss} by 0.5 to 0.7 eV (252-C and 252-B, respectively).

The perturbation of adding Mn nearest neighbors to create Mn-rich 171 and 252 NMC affects the range of computed values of ΔG_{diss}. The cation with the largest range of ΔG_{diss} is Mn (5.31 eV), while Ni has the smallest range (3.62 eV). For Ni and Co, there is clearly a correlation between the number of Mn nearest neighbors and predicted cation release; the more Mn surrounding either Ni or Co, the more likely it is to leave the surface. This trend is not as clear-cut for Mn because of the wider range of predicted ΔG_{diss} for atoms in similar chemical environments. Using the ΔG_{diss} at pH 3 (Table 1), one can compare tendencies for surface release by computing averages and standard deviations from that average. The analysis of average values taken from Table 1 shows that the free energy of Ni release from the 171, 252, and 333-NMC surfaces is -6.26 $\pm$ 0.22 eV, -5.21 $\pm$ 0.27 eV, and -2.81 eV, respectively, while for Mn the ΔG_{diss} are -5.81 $\pm$ 0.60 eV, -3.89 $\pm$ 0.27 eV, and -1.28 eV, respectively. The standard deviation of Mn ΔG_{diss} from 171-NMC is more than twice that of Ni.

A graphical depiction of ΔG_{diss} of Ni, Co, and Mn at pH 6, from 1/3 H-terminated NMC surfaces, is plotted as a function of nearest neighbors in Figure 5. This shows a similar trend for Ni, Co, and Mn; as the number of Mn nearest neighbors decreases from left to right, ΔG_{diss} increases. The increase in ΔG_{diss} can be further decomposed into 171, 252, and 333-NMC compositions. On average, metal release is predicted to occur for all cations in order of increased Mn content. In other words, ΔG_{diss} for the NMC compositions increases for $171 > 252 > 333$. The question to pose then is "Why is ΔG_{diss} more negative for compositions NMC-171 and NMC-252 than NMC 333?"

One way to approach answering this question is to decompose ΔG_{diss} into its constituent pieces, ΔG_1 and ΔG_2. ΔG_2 does not change between various NMC compositions, so the cation release trends must be related to ΔG_1. ΔG_1 is the DFT-computed energies of surface TM-OH vacancies,

so it informs us about relative lattice stabilities of the surface slab after a TM-OH unit has been removed. This implies that ΔG_1 can be used as a metric to determine how stable release products are relative to one another. For example, comparing Ni-OH release from 1/3H-covered NMC-171-A, NMC-252-A, and NMC-333 surfaces, ΔG_1 are 9.38, 10.41, and 12.58 eV, respectively. It is easiest to remove surface Ni from NMC-171-A, and hardest to remove from NMC-333. For Mn-OH release, ΔG_1 are 11.72, 13.36, and 15.99 eV for 1/3H-covered NMC-171-A, NMC-252-A, and NMC-333 surfaces, respectively. It is easiest to remove surface Mn from NMC-171-A, and hardest to remove from NMC-333. This type of comparison also means that it will be more favorable to remove a surface Ni-OH from NMC-252-A than a surface Mn-OH from NMC-171-A, which has been shown experimentally.[6]

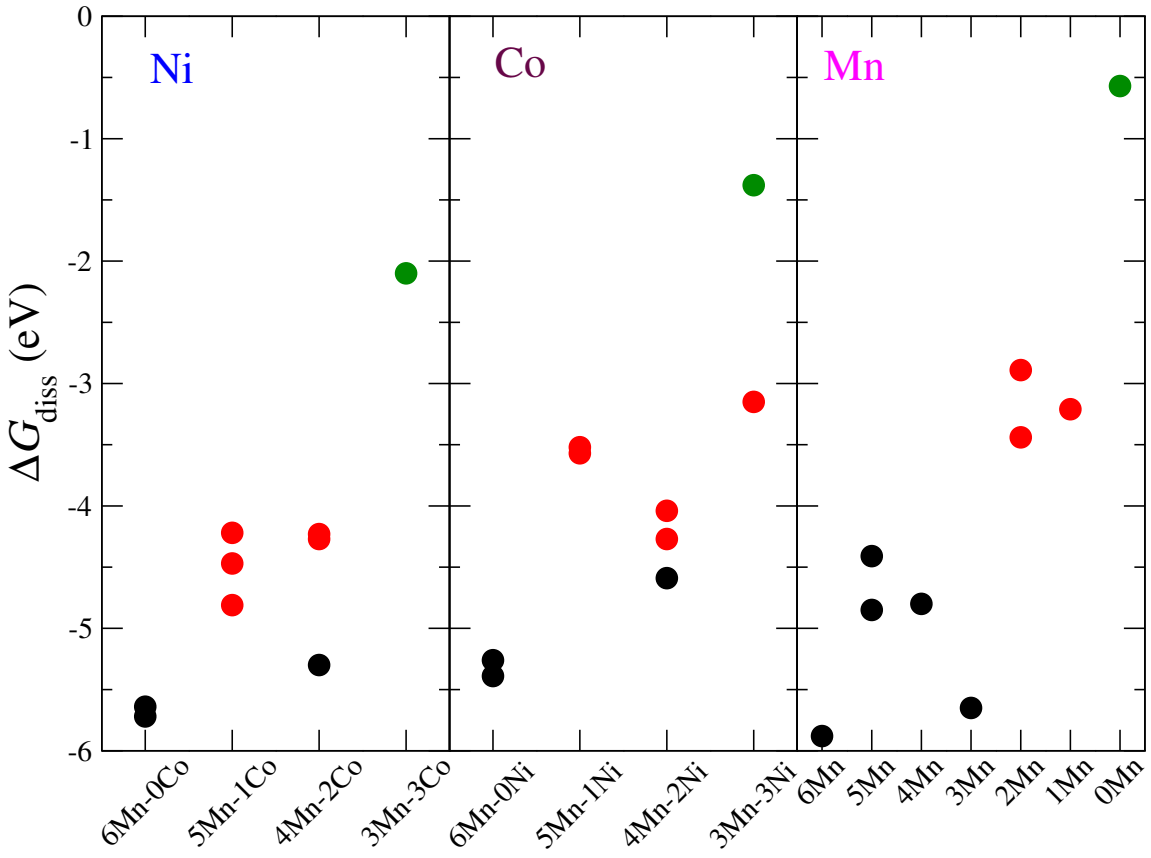

Figure 5: ΔG_{diss} of Ni, Co, and Mn from 1/3 H-terminated surfaces of NMC-171 (black), NMC-252 (red), and NMC-333 (green) as a function of nearest neighbors.

Projected density of states of Mn-rich NMC

To understand why ΔG_1 of NMC varies as a function of compositional tuning, we turn to analyses of the electronic band structure. An atom by atom, state by state projected density of states (PDOS) was done, in which the Kohn-Sham orbitals are projected onto atomic orbitals (centered on the atoms) in the CMO to interpret bonding interactions and TM oxidation state. The PDOS presented here correspond to the projection of $3d$ orbitals of specific TM (Ni, Mn, Co) on the DOS. In Figures 6 and 7, crystal field split diagrams (associated with the octahedral symmetry of the TM in NMC) are shown on the left hand side and PDOS are shown on the right hand side. The PDOS of NMC-171-A are shown in for Ni and Co in Figure 6a and for Mn in Figure 6b, for both 1/3 and 2/3 H surface coverage.

An example of how PDOS can be correlated to oxidation state is depicted in Figure 6 for NMC-171-A. In this structure, Ni and Co are nearest neighbors, and Ni is initialized in a spin-down configuration. For both the 2/3 and 1/3 H coverage, Ni is Ni^{2+}. In Figure 6a, the spin down state (green) of Ni is empty above E_F, the red line at Energy = 0 eV, and the spin up state (blue) has character both above (e_g) and below (t_{2g}) E_F. This is consistent with a d^8 electron configuration like Ni^{2+}, as shown in the crystal field split diagram to the left of the PDOS of Ni. Co is Co^{3+} because a low spin d^6 Co would have both the symmetric spin up/down t_{2g} character observed here, as well as e_g states above and below E_F for both up and down spin. This correlates to the crystal field split diagram to the left of the PDOS for Co.

The Mn PDOS in Figure 6b shows two distinct types of Mn in the 171-A surface, which are most likely Mn^{2+} and Mn^{4+}. Reducing Mn^{4+} to Mn^{2+} will populate the (green) spin down e_g states, shifting their location relative to E_F. Mn^{2+} will have a majority of spin down population below E_F, while Mn^{4+} will have spin down character both below and above E_F. Mn^{4+} has a d^3 electron configuration, which will result in empty spin-up states, where both t_{2g} and e_g are above E_F, and half-filled spin-down states, where only e_g is above E_F and t_{2g} is below. A high spin Mn^{2+} (initialized spin down) will have a d^5 electron configuration where the spin down states are completely filled (t_{2g} and e_g states are below E_F) and the spin up states are empty (t_{2g} and e_g states

are both above E_F). This is best observed in the PDOS of the 1/3 H terminated 171-A surface, where the majority of band character of the spin down configuration (green) is below E_F, and the majority of spin up band character are above E_F.

The PDOS also show that changing the chemical environment, via surface terminations, will change the oxidation state of the surface transition metals. What changes most as a function of surface coverage is the relative amounts of Mn^{2+} and Mn^{4+}. For example, in NMC 171-A, the surface with 2/3 H coverage has 5 Mn^{2+} and 2 Mn^{4+}, while the surface 1/3 H coverage has 3 Mn^{2+} and 4 Mn^{4+}. The surface with less H coverage requires more surface Mn^{4+}, so decreasing H surface coverage results in oxidation of surface Mn. Previous DFT investigations on 333 NMC showed that as surface terminations change, the first element to reduce/oxidize is Ni. Here, compositional tuning to create Mn-rich NMC has ensured that Mn will be the first to experience changes in oxidation state as a function of changes in coordination environment.

Comparison of the PDOS in Figure 6 also shows that adjusting the surface terminations of NMC 171-A from 1/3 to 2/3 H will not affect the oxidation state of Ni and Co (right hand side of Figure 5a) as much as it does Mn (right hand side of Figure 5b). The change in 3*d* character in the (green) spin-up channel of both Mn^{4+} and Mn^{2+} is most affected by surface termination; at lower H-coverage each has two large bands beneath E_F, and at high H-coverage, at least four bands are present beneath E_F.

The behavior of the Ni, Co, and Mn PDOS in Figure 7 are similar to those in Figure 6, except that the spin down channel of Mn^{4+} (blue) is metallic for Mn-rich NMC composition 171-A (both 2/3 and 1/3 H surface coverages) and insulating for the 252-A composition (both 2/3 and 1/3 H surface coverage). In addition, the decrease in population above E_F is smaller for the 252-A surface, for both H-surface coverage values. Analysis of the PDOS of Mn-rich NMC compositions clearly shows that Mn spin state is highly variable, and able to change as a function of composition and surface termination. This is in agreement with the trends in ΔG_{diss} presented in Figures 3 and 4.

Table 2 shows two different possible oxidation states of Mn, labeled MnA and MnB. MnA and

Table 2: 3*d* electron count for the occupied states of 171 and 252-NMC, for 1/3 and 2/3H surface coverage.

	171				252			
	1/3H		2/3H		1/3H		2/3H	
TM	Down	Up	Down	Up	Down	Up	Down	Up
Ni	4.90	3.43	4.92	3.43	4.90	3.43	4.92	3.43
Co	3.67	3.71	3.68	3.71	3.67	3.70	3.66	3.72
MnA	3.83	1.44	3.74	1.58	3.93	1.23	3.82	1.47
MnB	4.57	0.66	4.47	0.73	4.19	0.96	4.37	0.84

MnB have spin down and spin up 3*d*-electron counts of 3.83 and 1.44, and 4.57 and 0.66 for 1/3H-covered 171-NMC surfaces. Changing surface coverage, from 1/3 to 2/3 H, and/or composition, from 171 to 252-NMC, only changes the 3*d* electron count of each species by $\approx$ 0.1-0.3. This implies that MnA and MnB remain distinct from each other for the range of chemical environments investigated here. On average, MnA has between 3.74-3.93 spin up 3*d*-electrons and 1.58-1.23 spin down 3*d*-electrons. Since the *d*-electron count of Co^{3+} is $\approx$ 3.70 and spin down Ni^{2+} is 3.43, one can assign MnA to have 3 spin-down *d*-electrons, consistent with Mn^{4+} or low-spin Mn^{3+}. Compared to MnA, MnB has more spin-down *d*-electrons and less spin-up *d*-electrons, however, the total number *d* of electrons per Mn only varies between 5.15 (MnB, 1/3H coverage of 252-NMC) and 5.32 (MnA, 2/3H coverage of 171-NMC). Changing surface coverage and composition results in a redistributes of Mn electron density, such that MnB is consistent with Mn^{2+} or low-spin Mn^{3+}. A detailed discussion of Table 2 can be found in Section S2 of the online supplemental materials.

Changes in Mn spin states

In order to differentiate the spin states for each Mn, we turn to the DFT-computed electronic structure, where we are able to compute the spin on each atom. Figure 8 illustrates how the magnetic moment of Mn atoms changes as a function of composition, surface termination, and cation release, and how this can be used as a guide for determining the populations of Mn^{2+} and

Mn^{4+} in the surface. One can use the basic spin equation formula to relate the observed magnetic moment of an isolated ion to the number of spins, s, in units of μB. Here the DFT-computed spin, s, can be broken into the total number of unpaired electrons using the formula $s = \sqrt{e_s(e_s+1)}$, where e_s is 1/2. In this formula, 5 unpaired e- have 2.95 μB, indicative of high-spin Mn^{2+}, 4 unpaired e- have 2.45 μB, indicative of Mn^{3+}, and 3 unpaired e- have 1.94 μB, indicative of Mn^{4+}. Since Mn-rich NMC is a CMO material, and the Mn are in different bonding environments that are influenced by their neighboring atoms, it is expected that there will be changes in computed Mn spins relative to the isolated spin values reported above; however, the Mn spin states that we have already postulated in the PDOS presented in the previous section (Mn^{2+} and Mn^{4+}) will be separated by $\approx$1 μB.

Here we analyze the general trends in DFT-computed magnetic moments by computing average values of the grouped points in Figure 8. The magnetic moments of Mn-rich NMC 171 compositions shows two distinct Mn spin populations (black dots, left hand side of Figure 8a) that change as a function of surface termination. For 2/3 H surface coverage the average values are 3.26 (MnB) and 1.86 μB (MnA), and for 1/3 H surface coverage they change to average values of 3.01 and 2.00 μB (black dots, right hand side of Figure 8a). The values for this surface coverage of NMC-171 are close to those observed in 2/3 H surface coverage of Mn-rich 252 compositions (black dots, left hand side of Figure 8b); where the average values of 3.07 and 2.03 μB. Decreasing H-surface coverage of 252 compositions from 2/3 to 1/3 adjusts the average value of magnetic moment even further, to 2.94 and 2.26 μB. For the 1/3 H surface coverage of 252, the difference between the high and low values of Mn spin is smallest, but each of the sets of data seems to be moving towards an overall average of $\approx$2.5μB, which would be an overall average associated with Mn^{3+}. Analysis of the spins of MnA and MnB allow for assignment to oxidation states consistent with Mn^{4+} and Mn^{2+}, respectively, and that changing the surface coverage and composition will lead to changes in the surface Mn.

Also shown in Figure 8 are the Mn spin moments after release of a transition metal species (red dots). For both 171 surface coverages, and the 2/3 H covered 252 surface, two distinct spin popula-

tions are observed, while for the 1/3 H covered 252 surface, the spins merge into a continuum. This indicates that for all Mn-rich NMC surfaces, even after initial TM-OH release events take place, Mn^{2+} is still present to interrupt the preferred spin-lattice and bonding interactions observed in NMC-333.

The analysis of computed Mn spin states in compositionally tuned NMC relates directly to recent experimental work. Here, we determine that the increased amount of Mn^{2+} relative to Mn^{4+} destabilizes Mn-rich NMC compositions, facilitating enhanced release of Ni, Co, and Mn when compared to NMC-333. These findings generally agree with an ICP-OES analysis of Mn-rich NMC, where it was shown that NMC [6] compositions with higher Mn content released increased amounts of Mn relative to Ni and Co.

Metal Oxidation State as a Function of Compositional Tuning

Table 3: Oxidation states of Ni, Co, and Mn in NMC compositions as a function of H surface coverage. Mn oxidation states are given as the ratio of Mn^{2+}:Mn^{4+}. A - in the Mn-ratio columns indicate that only Mn^{4+} is observed.

	Ni		Co		Mn-ratio	
	2/3H	1/3H	2/3H	1/3H	2/3H	1/3H
171-A	Ni^{2+}	Ni^{2+}	Co^{3+}	Co^{3+}	5:2	3:4
171-B	Ni^{2+}	Ni^{2+}	Co^{2+}	Co^{3+}	3:4	3:4
171-C	Ni^{2+}	Ni^{2+}	Co^{2+}	Co^{3+}	3:4	3:4
252-A	Ni^{2+}	Ni^{2+}	$Co^{2+/3+}$	Co^{3+}	3:2	2:3
252-B	Ni^{2+}	Ni^{2+}	$Co^{2+/3+}$	Co^{3+}	3:2	2:3
252-C	Ni^{2+}	Ni^{2+}	$Co^{2+/3+}$	Co^{3+}	3:2	2:3
333-A	$Ni^{2+/3+}$	Ni^{2+}	Co^{3+}	Co^{3+}	-	-

In general, the results of the DFT + solvent ion model show an increased amount of Mn^{2+} at higher H coverage, and that the surface cation redox sensitivity as a function of surface coverage is clearly linked to changes in composition. Table 3 lists how the oxidation states of Ni, Co, and Mn change as a function of surface coverage and composition. Comparing the NMC 252, 171, and 333 compositions, surface Ni does not exhibit redox sensitivity as a function of H coverage for either Mn-rich composition, but will for NMC-333. The values in Table 3 indicate that surface

Ni will reduce/oxidize above levels of x=22% Ni. At similar Co levels (x=22% Co), at least one of the two Co in the 252 surface will reduce to Co^{2+}. At lower H-coverage, both Co are Co^{3+}.

For a more atomistic description of how composition can influence redox behavior, we can compare the NMC 171 values in Table 3. In NMC 171-A, when Ni and Co are nearest neighbors, what changes as a function of surface coverage is the ratio of Mn^{2+}/Mn^{4+}, while $Ni^{2Co}_{4[Mn}$ and Co^{2Ni}_{4Mn} remain Ni^{2+} and Co^{3+}, respectively. As stated in the previous section, less H coverage results in more Mn^{4+} than Mn^{2+}. For NMC 171-B and 171-C, when Ni and Co are not nearest neighbors (separated by at least one Mn), Ni is Ni^{2+} for both surface coverages, but Co is Co^{2+} for 2/3 H coverage and Co^{3+} for 1/3 H coverage. The ratio of Mn^{2+}: Mn^{4+} remains the same for both H surface coverages in these example surfaces. This is an illustration of how changing the surface termination is coupled to changing the composition: changes the oxidation state of the surface Co will occur when it is not next to a Ni. A Co cation that will be easier to release from the surface is created in this instance, since Co^{2+} is stable aqueous species. This also implies that the isolated Co^{0Ni}_{6Mn} in NMC 171-B and 171-C will have similar environmentally dependent behavior.

Conclusions

We use a DFT + solvent ion method to investigate compositional variations of $Li_xNi_yMn_zCo_{1-y-z}O_2$, a CMO used in LIBs. We find that the surface release of TM from CMOs are highly dependent upon changes in both composition and surface functional groups, and predict that enriching NMC with Mn will destabilize the solid solution relative to equistoichiometric NMC compositions. We demonstrate that one can use DFT to obtain metrics to gauge the effects of compositional tuning of CMOs, specifically ΔG_{diss} and PDOS. The PDOS, which are used to differentiate between Mn^{2+} and Mn^{4+}, can be correlated to crystal field split models, and are generally in good agreement. A spin state analysis, coupled to the PDOS, shows that metal release is influenced by composition and surface coverage, and that redox sensitivity is influenced by both sets of design parameters. In other words, the TM oxidation state affects the stability of the TM in the lattice and its tendency to form a hydrated cation; both overall stoichiometry (composition) and local structure (surface

functional groups) govern the TM oxidation states in the CMO. The transformations investigated here, for a wide-range of NMC compositional variants, can also be used to redesign CMO nanomaterials because it serves as a platform for how compositional tuning will affect the interplay of redox properties, oxidation state, and coordination environment. Moreover, the incongruent pH-dependant cation release trends can be used as input data to refine environmental fate and/ toxicity models for CMOs.

To comment further on the redesign of CMOs: the Mn-rich NMC surfaces investigated here are unstable relative to NMC-333 compositions. This is because the introduction of Mn^{2+} in the Mn-rich NMC compositions interrupts the spin and lattice interactions of the surrounding TM, relative to the perfectly alternating NMC-333 surfaces. However, this may not be detrimental if one of the design criteria is to create a cathode material whose purpose at end of life is to readily release cations that can be recycled after use. If not, then one route to mitigate TM release from Mn-rich NMC, or protect against oxide dissolution in general, would be to form protective coatings. One example of this scheme could be from binding environmentally available small molecules[41] such as phosphate to the surface. Phosphate is a major component of industrial coatings such as LiPON[42] and metal-phosphates,[43–45] and can be found in non-flammable thiophosphate solid electrolytes.[46]

Associated Content

The Supporting Information is available free of charge on the ACS Publications website at DOI:xxxx Presented in the Supporting Information are thermodynamic tables, example release cycles, and an extended PDOS discussion.

Author Information

Corresponding Author: sara-mason@uiowa.edu

Notes: The authors declare no competing financial interest.

Acknowledgments

This work was supported by National Science Foundation Center under the Center for Sustainable Nanotechnology, CHE-1503408. The CSN is part of the Centers for Chemical Innovation Program. This research was supported in part through computational resources provided by The University of Iowa, Iowa City, Iowa and the National Science Foundation grant CHE-0840494. This work used the Extreme Science and Engineering Discovery Environment (XSEDE[47]), which is supported by National Science Foundation grant number ACI-1548562 through allocation ID TG-GEO160006. J.W.B., D.J. and S.E.M. thank Blake Hudson, Profs. Christy Haynes, Qiang Cui and Rigoberto Hernandez for useful discussions of this work.

References

(1) Narins, T. P. The battery business: Lithium availability and the growth of the global electric car industry. *Extractive Industries and Society* **2017**, *4*, 321–328.

(2) Olivetti, E. A.; Ceder, G.; Gaustad, G. G.; Fu, X. Lithium-Ion Battery Supply Chain Considerations: Analysis of Potential Bottlenecks in Critical Metals. *Joule* **2017**, *1*, 229–243.

(3) Hamers, R. J. Nanomaterials and Global Sustainability. *Acc. Chem. Res.* **2017**, *50*, 633–637.

(4) Hang, M. N.; Gunsolus, I. L.; Wayland, H.; Melby, E. S.; Mensch, A. C.; Hurley, K. R.; Pedersen, J. A.; Haynes, C. L.; Hamers, R. J. Impact of Nanoscale Lithium Nickel Manganese Cobalt Oxide (NMC) on the Bacterium Shewanella oneidensis MR-1. *Chem. Mater.* **2016**, 1092–1100.

(5) Dogangun, M.; Hang, M. N.; Machesky, J.; McGeachy, A. C.; Dalchand, N.; Hamers, R. J.; Geiger, F. M. Evidence for Considerable Metal Cation Concentrations from Lithium Inter-

calation Compounds in the Nano-Bio Interface Gap. *J. Phys. Chem. C.* **2017**, *121*, 27473–27482.

(6) Gunsolus, I. L.; Hang, M. N.; Hudson-Smith, N. V.; Buchman, J. T.; Bennett, J. W.; Conroy, D.; Mason, S. E.; Hamers, R. J.; Haynes, C. L. Influence of nickel manganese cobalt oxide nanoparticle composition on toxicity toward *Shewanella oneidensis* MR-1: redesigning for reduced biological impact. *Environ. Sci.: Nano.* **2017**, *4*, 636–646.

(7) Bozich, J.; Hang, M.; Hamers, R. J.; Klaper, R. Core chemistry influences the toxicity of multicomponent metal oxide nanomaterials, lithium nickel manganese cobalt oxide, and lithium cobalt oxide to *Daphnia magna*. *Environ. Toxicology and Chem.* **2017**, *36*, 2493–2502.

(8) Arvidsson, R. Risk Assessments Show Engineered Nanomaterials to be of Low Environmental Concern. *Environ. Sci. Technol.* **2018**, *52*, 2436–2437.

(9) Musee, N. Comment on "Risk Assessments Show Engineered Nanomaterials to be of Low Environmental Concern". *Environ. Sci. Technol.* **2018**, *52*, 6723–6724.

(10) Nel, A.; and, T. X. Nanomaterial Toxicity Testing in the 21st Century: Use of a Predictive Toxicological Approach and High-Throughput Screening. *Acct. Chem. Res.* **2013**, *46*, 607–619.

(11) Keller, A. A.; McFerran, S.; Lazareva, A.; Suh, S. Global life cycle releases of engineered nanomaterials. *J. Nanoparticle Res.* **2013**, *15*, 1692.

(12) Sun, T. Y.; Mitrano, D. M.; Bornhoft, N. A.; Scheringer, M.; Hungerbuhler, K.; Nowack, B. Envisioning Nano Release Dynamics in a Changing World: Using Dynamic Probabalistic Modeling to Assess Future Environmental Emissions of Engineered Nanomaterials. *Environ. Sci. Technol.* **2017**, *51*, 2854–2863.

(13) Giese, B.; Klaessig, F.; Park, B.; Kaegi, R.; Steinfeldt, M.; Wigger, H.; von Gleich, A.;

Gottschalk, F. Risks, Release and Concentrations of Engineered Nanomaterial in the Environment. *Scientific Reports* **2018**, *8*, 1565–1–18.

(14) Yuan, C.; Wu, H. B.; Xie, Y.; Lou, X. W. Mixed Transition-Metal Oxides: Design, Synthesis, and Energy-Related Applications. *Angew. Chem. Int. Ed.* **2014**, *53*, 1488–1453.

(15) Chen, D.; Chen, C.; Baiyee, Z. M.; Shao, Z.; Ciucci, F. Nonstoichiometric Oxides as Low-Cost and Highly-Efficient Oxygen Reduction/Evolution Catalysts for Low-Temperature ELectrochemical Devices. *Chem. Rev.* **2015**, *115*, 9869–9921.

(16) Hang, M. N.; Hudson-Smith, N. V.; Clement, P. L.; Zhang, Y.; Wang, C.; Haynes, C. L.; Hamers, R. J. Influence of Nanoparticle Morphology on Ion Release and Biological Impact of Nickel Manganese Cobalt Oxide (NMC) Complex Oxide Nanomaterials. *ACS Appl. Nano Mater.* **2018**, *10.1021/acsanm.8b00187*.

(17) Zhang, K.; Schnoor, J. L.; Zeng, E. Y. E-Waste Recycling: Where Does It Go from Here? *Environ. Sci. Technol.* **2012**, *46*, 10861–10867.

(18) Billy, E.; Joulie, M.; Laucournet, R.; Boulineau, A.; DeVito, E.; Meyer, D. Dissolution Mechanisms of LiNi1/3Mn1/3Co1/3O2 Positive Electrode Material from Lithium-Ion Batteries in Acid Solution. *ACS Appl. Mater. Interfaces* **2018**, *10*, 16424–16435.

(19) Han, L.; Dong, S.; Wang, E. Transition-Metal (Co, Ni, and Fe)-Based Electrocatalysts for the Water Oxidation Reaction. *Adv. Mater.* **2016**, *28*, 9266–9291.

(20) Chang, F.; Shen, J.; Peng, B.; Pan, Y.; Tao, Z.; Chen, J. Rapid room-temperature synthesis of nanocrystalline spinels as oxygen reduction and evolution electrocatalysts. *Nature Chem.* **2011**, *3*, 79–84.

(21) Liang, Y.; Wang, H.; Zhou, J.; Li, Y.; Wang, J.; Reiger, T.; Dai, H. Covalent Hybrid of Spinel Manganese-Cobalt Oxide and Graphene as Advanced Oxygen Reduction Electrocatalysts. *J. Am. Chem. Soc.* **2012**, *134*, 3517–3523.

(22) Barnard, A. S. How can *ab initio* simulations address risks in nanotech? *Nature Nanotech.* **2009**, *4*, 332–335.

(23) Winkler, D. A. Recent advances, and unresolved issues, in the application of computational modeling to the prediction of the biological effects of nanomaterials. *Toxic. and Appl. Pharma.* **2016**, *299*, 96–100.

(24) Manshian, B. B.; Pokhrel, S.; Himmelreich, U.; Tamm, K.; Sikk, L.; Fernandez, A.; Rallo, R.; Tamm, T.; Madler, L.; Soenen, S. J. In Silico Design of Optimal Dissolution Kinetics of Fe-Doped ZnO Nanoparticles Results in Cancer-Specific Toxicity in a Preclinical Rodent Model. *Adv. Healthcare Mater.* **2017**, *6*, 1001379–1–11.

(25) Rong, X.; Kolpak, A. M. Ab initio Approach for Prediction of Oxide Surface Structure, Stoichiometry, and Electrocatalytic Activity in Aqueous Solution. *Phys. Chem. Lett.* **2015**, *6*, 1785–1789.

(26) Huang, X.; Bennett, J. W.; Hang, M. N.; Laudadio, E. D.; Hamers, R. J.; Mason, S. E. *Ab initio* Atomistic Thermodynamics Study of the (001) Surface of $LiCoO_2$ in a Water Environment and Implications for Reactivity under Ambient Conditions. *J. Phys. Chem. C.* **2017**, *121*, 5069–5080.

(27) Bennett, J. W.; Jones, D.; Huang, X.; Hamers, R. J.; Mason, S. E. Dissolution of complex metal oxides from first-principles and thermodynamics: Cation removal from the (001) surface of $Li(Ni_{1/3}Mn_{1/3}Co_{1/3})O2$. *Environ. Sci. Technol.* **2018**, *10.1021/acs.est.8b00054*.

(28) Dale, A. L.; Casman, E. A.; Lowry, G. V.; Lead, J. R.; Viparelli, E.; Baalousha, M. Modeling Nanomaterial Environmental Fate in Aquatic Systems. *Environ. Sci. Technol.* **2015**, *49*, 2587–2593.

(29) Dale, A. L.; Lowry, G. V.; Casman, E. A. Stream Dynamics and Chemical Transformations Control the Environmental Fate of Silver and Zinc Oxide Nanoparticles in a Watershed-Scale Model. *Environ. Sci. Technol.* **2015**, *49*, 7285–7293.

(30) Hohenberg, P.; Kohn, W. Inhomogeneous Electron Gas. *Phys. Rev.* **1964**, *136*, B864–71.

(31) Kohn, W.; Sham, L. J. Self-Consistent Equations Including Exchange and Correlation Effects. *Phys. Rev.* **1965**, *140*, A1133–8.

(32) Giannozzi, P.; Baroni, S.; Bonini, N.; Calandra, M.; Car, R.; Cavazzoni, C.; Ceresoli, D.; Chiarotti, G. L.; Cococcioni, M.; Dabo, I.; et al., Quantum ESPRESSO: A Modular and Open-Source Software Project for Quantum Simulations of Materials. *J. Phys.:Condens. Matter* **2009**, *21*, 395502–20.

(33) Vanderbilt, D. Soft Self-Consistent Pseudopotentials in a Generalized Eigenvalue Formalism. *Phys. Rev. B Rapid Comm.* **1990**, *41*, 7892–5.

(34) Garrity, K. F.; Bennett, J. W.; Rabe, K. M.; Vanderbilt, D. Pseudopotentials for high-throughput DFT calculations. *Comp. Mater. Sci.* **2014**, *81*, 446–452.

(35) Perdew, J. P.; Burke, K.; Ernzerhof, M. Generalized Gradient Approximation Made Simple. *Phys. Rev. Lett.* **1996**, *77*, 3865–8.

(36) Corum, K. W.; Huang, X.; Bennett, J. W.; Mason, S. E. Systematic Density Functional Theory Study of the Structural and Electronic Properties of Constrained and Fully Relaxed (001) Surfaces of Alumina and Hematite. *Molecular Simulation* **2017**, *43*, 406–419.

(37) Monkhorst, H. J.; Pack, J. D. Special Points for Brillouin-Zone Integrations. *Phys. Rev. B* **1976**, *13*, 5188–5192.

(38) Rong, X.; Parolin, J.; Kolpak, A. M. A Fundamental Relationship between Reaction Mechanism and Stability in Metal Oxide Catalysts for Oxygen Evolution. *ACS Catal.* **2016**, *6*, 1153–1158.

(39) Wagman, D. D. E.; Halow, I.; Parker, V. B.; Bailey, S. M.; Schumm, R. H. Selected Values of Chemical Thermodynamic Properties. *National Bureau of Standards* **1971**,

(40) Persson, K. A.; Waldwick, B.; Lazic, P.; Ceder, G. Prediction of solid-aqueous equilibria: Scheme to combine first-principles calculations of solids with experimental aqueous states. *Phys. Rev. B.* **2012**, *85*, 235438.

(41) Laudadio, E. D.; Bennett, J. W.; Mason, S. E.; Hamers, R. J. Phosphate Adsorption on Battery Cathode Nanomaterials Impacts Environmental Prescence and Bioavailability. *TBD* **2018**,

(42) Kim, Y.; Veith, G. M.; Nanda, J.; Unocic, R. R.; Chi, M.; Dudney, N. J. High Voltage Stability of $LiCoO_2$ Particles with a Nanoscale Lipon Coating. *Electrochim. Acta.* **2011**, *56*, 6573–6580.

(43) Lu, Y.-C.; Mansour, A. N.; Yabuuchi, N.; Shao-Horn, Y. Probing the Origin of Enhanced Stability of $AlPO_4$ Nanoparticle Coated $LiCoO_2$ during Cycling to High Voltages: Combined XRD and XPS Studies. *Chem. Mater.* **2009**, *21*, 4408–4424.

(44) Cho, J.; Lee, J.-G.; Kim, B.; Park, B. Effect of P_2O_5 and $AlPO_4$ Coating on $LiCoO_2$ Cathode Material. *Chem. Mater.* **2003**, *15*, 3190–3193.

(45) Lee, J.-G.; Kim, T.-G.; Park, B. Metal-Phosphate Coating on $LiCoO_2$ Cathodes with High Cutoff Voltages. *Mater. Res. Bull.* **2007**, *42*, 1201–1211.

(46) Richards, W. D.; Miara, L. J.; Wang, Y.; Kim, J. C.; Ceder, G. Interface Stability in Solid-State Batteries. *Chem. Mater.* **2016**, *28*, 266–273.

(47) Towns, J.; Cockerill, T.; Dahan, M.; Foster, I.; Gaither, K.; Grimshaw, A.; Hazlewood, V.; Lanthrop, S.; Lifka, D.; Peterson, G. D.; Roskies, R.; Scott, J. R.; Wilkins-Diehr, N. XSEDE:Accelerating Scientific Discovery. *Comp. Sci. Engineering* **2014**, *16*, 62–74.

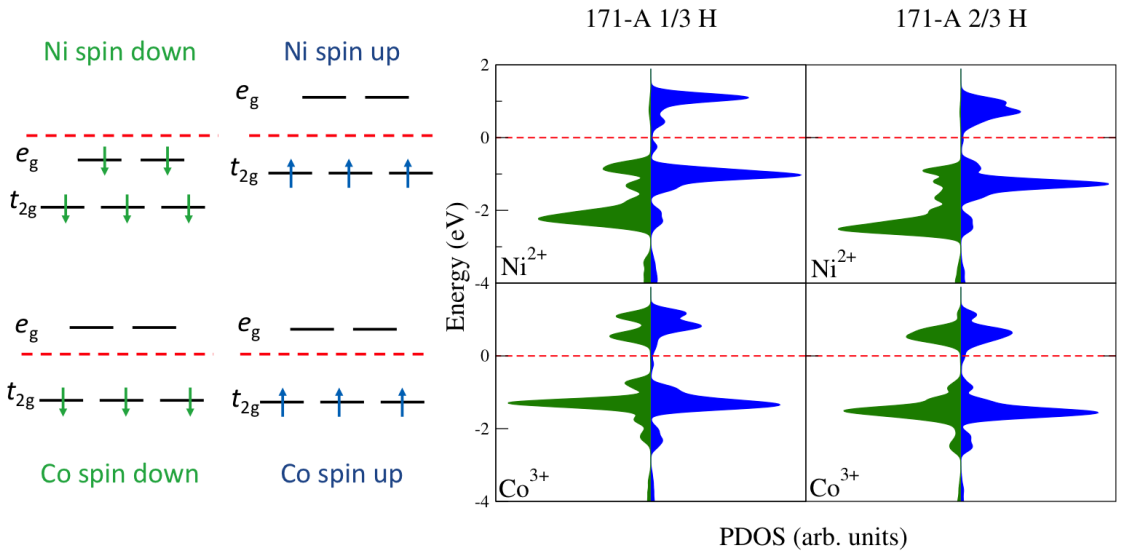

(a)

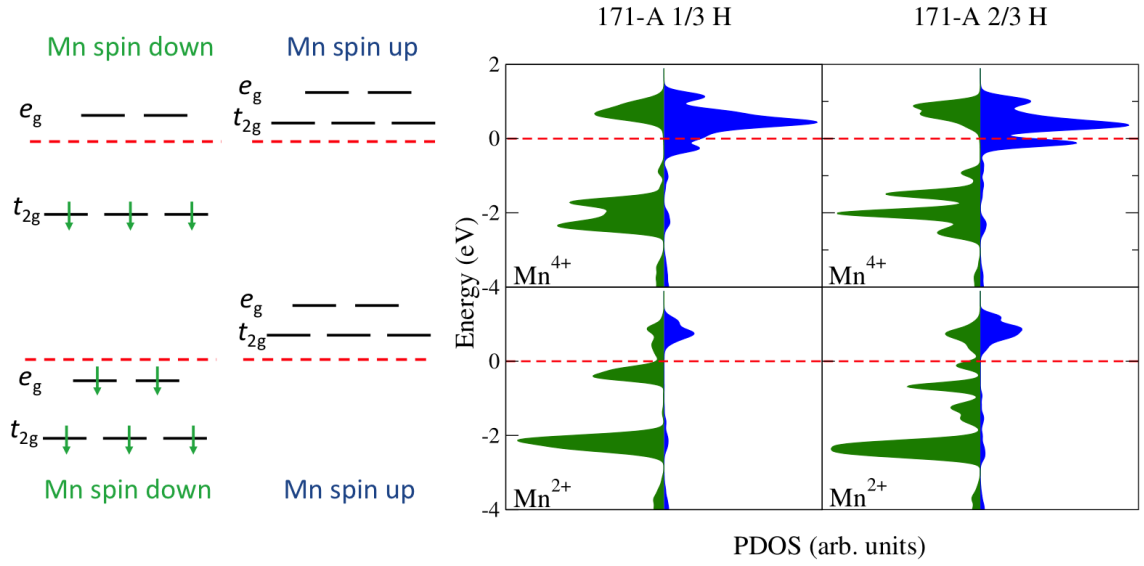

(b)

Figure 6: Left: Schematic octahedral crystal field splitting diagram for Ni^{2+} and Co^{3+} (a) and Mn^{4+} and Mn^{2+} (b). Right: PDOS of Mn-rich NMC surface 171-A for a) Ni and Co and b) Mn. For all plots, the spin down density is green and the spin up density is blue.

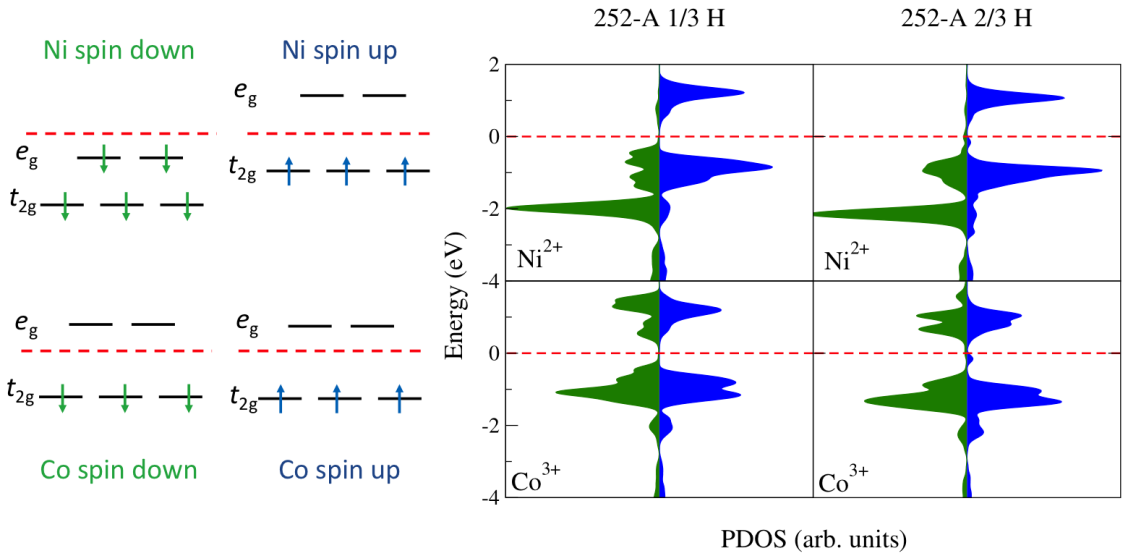

(a)

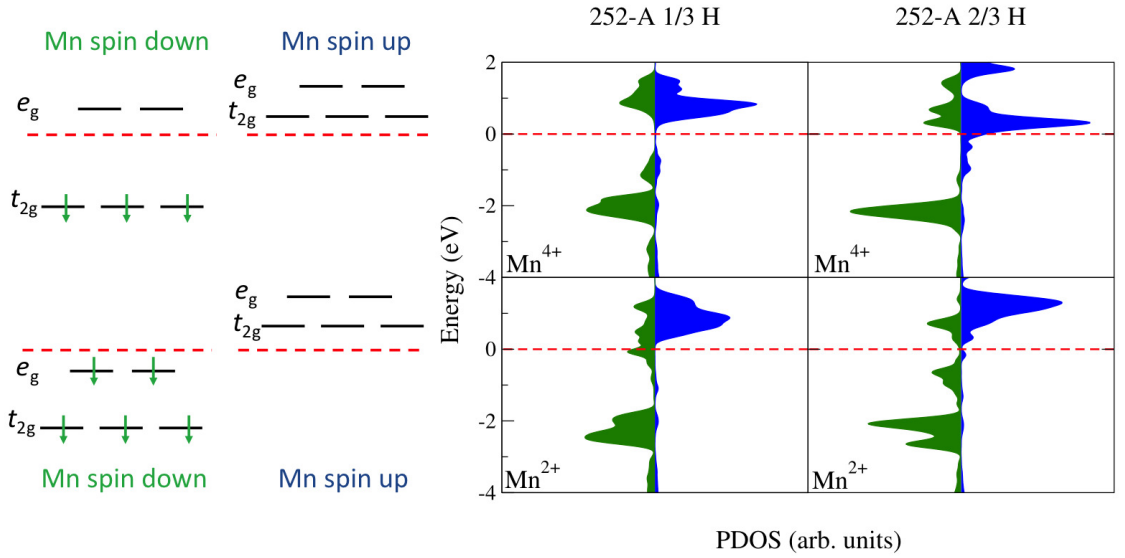

(b)

Figure 7: Same descriptions as Figure 5 for Mn-rich NMC surface 252-A.

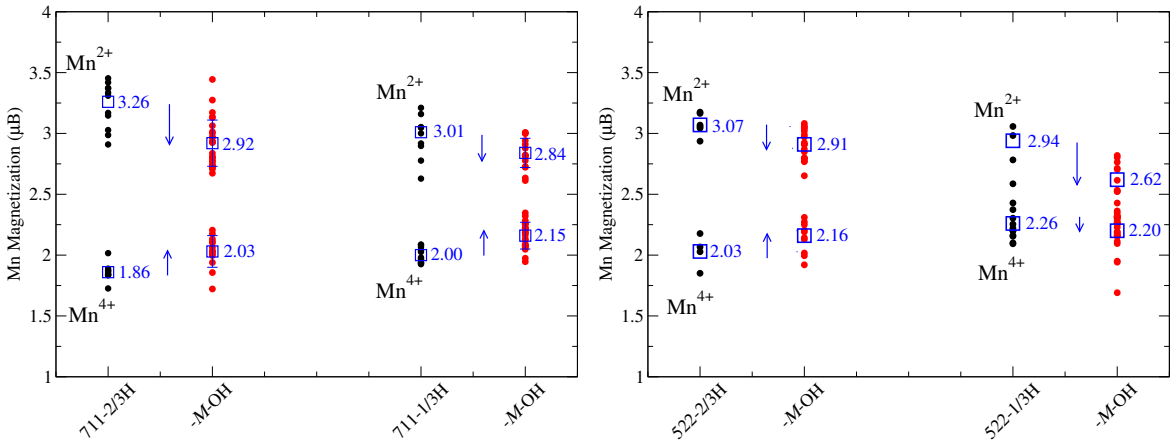

(a) 171 (b) 252

Figure 8: Plots of calculated Mn magnetic moment in μB. Left side are the 171-NMC surfaces and right side are the 252-NMC surfaces. The magnetic moments of Mn changes for the surfaces both before (black circles) and after (red circles) metal release and are split into two sets, indicative of both Mn^{2+} and Mn^{4+} present in the surface.

For Table of Contents Only

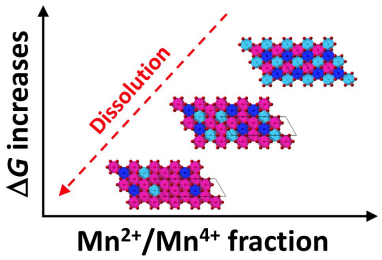

Figure 9: Synopsis: Enriching complex metal oxides with inexpensive, Earth abundant, and environmentally friendly elements via compositional tuning is a promising design strategy to explore new sustainable nanomaterials for energy storage technologies. We compute the thermodynamics of dissolution of a compositionally-tuned complex metal oxide and find that the release of transition metals from the surface is mediated by the interplay of coordination environment, oxidation state, and surface coverage.